Article:
Quan, G., Huang, S. and Burgess, I. (2016) Component-based model of buckling panels of steel beams at elevated temperatures. Journal of Constructional Steel Research, 118. pp. 91-104. ISSN: 0143-974X

https://doi.org/10.1016/j.jcsr.2015.10.024

Component-Based Model of Buckling Panels of Steel Beams at Elevated Temperatures

Guan Quan, Shan-Shan Huang, Ian Burgess

University of Sheffield, Department of Civil and Structural Engineering, UK

Abstract

Both bottom-flange buckling and beam-web shear buckling have been observed in many full-scale fire tests in the vicinity of beam-to-column connections. These phenomena can influence the load redistribution within the adjacent connections and the global structural behaviour, detrimentally affecting the structural overall fire resistance. However, existing models for bottom-flange buckling overestimate the structural resistance when the beam is slender. In this work, a new analytical model has been created to predict both of these types of buckling behaviour in steel beams in the vicinity of beam-to-column connections at elevated temperatures. The model considers the individual effects of both buckling modes, as well as their interaction. It is capable of predicting the force-deflection relationship of the buckling zone from the initial elastic loading stage to run-away failure. The new analytical model has been compared with the existing Dharma's model and a range of 3D finite element simulations created using the ABAQUS software. Comparisons have shown that the proposed method gives better predictions than Dharma's model. A component-based model of the buckling zone has been created on the basis of this new analysis. The component-based model can provide sufficient accuracy, and will be

implemented in the software Vulcan for performance-based global structural fire analysis.

Keywords: Shear Buckling; Bottom-Flange Buckling; Component-Based Model; Fire.

Notation:

b	flange width
c	half flange width
d	depth of a beam web
f	width of one strut in compression zone
F	vertical shear force at the end of the buckling zone
F_{max}	maximum reaction force
$F_{p,T}$	reaction force when plastic bending moment resistance is reached
h_c	height of the area resisting axial force in a strut
k_1	the stiffness of the compressive spring in the flange buckling component
k_2	the stiffness of the compressive spring in the shear buckling component
k_E	reduction factor for young's modulus at elevated temperatures
k_y	reduction factor for yield stress at elevated temperatures
M	bending moment at the end of the buckling zone
M_p	bending moment resistance of one beam-web compressive strut
P_c	axial force resistance of one beam-web compressive strut
t_f	thickness of the flange
t_w	thickness of the beam web
α	the angle between tensile strips and the deformed upper flange
α_1	the angle between a yield line and vertical direction
Δ_1	out-of-plane deflection of one strut
Δ_{vs}	the vertical movement of the right edge of the shear panel
$\varepsilon_{l,\theta}$	limiting strain for yield strength at elevated temperatures
$\varepsilon_{p,\theta}$	strain at the proportional limit at elevated temperatures
$\varepsilon_{u,\theta}$	ultimate strain of steel at elevated temperatures
$\varepsilon_{y,\theta}$	yield strain of steel at elevated temperatures
θ_1	the rotation caused by bottom-flange buckling
θ_2	the rotation caused by shear buckling
σ_c	compressive stress in the compressive strips
σ_{cf}	compressive stress in the flange along beam length
σ_{eq}	yield strength of the flange considering reduction caused by axial stresses and shear stresses
σ_{eq1}	yield strength of the flange considering reduction caused by axial stress parallel to yield lines
$\sigma_{p,\theta}$	stress at the proportional limit at elevated temperatures
σ_r	stress normal to the yield lines
σ_t	tensile stress in the tensile strips
σ_{tf}	tensile stress in the flange along beam length
σ_y	yield strength of steel at ambient temperature
$\sigma_{y,\theta}$	yield strength of steel at elevated temperatures
$\sigma_{yf,\theta}$	yield strength of the flange without considering reduction at elevated temperatures
$\sigma_{yw,\theta}$	yield strength of steel web at elevated temperatures
τ_r	shear force parallel to the yield lines

1. Introduction

The collapse of the '7 World Trade' building in New York City [1] indicates that the progressive collapse of the whole building was initially triggered by the failure of beam-to-column connections. Connection failure was also observed on many other occasions, including the well-known full-scale Cardington series of Fire Tests [2]. Beam-to-column connections have been among the key elements for the investigation of the robustness of steel structures in fire. It has traditionally been assumed that connections have sufficient fire resistance, because of their lower temperatures and slower rates of heating compared with the members to which they are connected. However, connections are actually under complicated and extreme force combinations transferred from the connected members; these forces are not usually considered in ambient-temperature design. A number of previous research studies [3-6] have shed light on the performance of beam-to-column connections in fire, and have further proved that connections are potentially the most vulnerable parts of a steel-framed structure in fire.

The Cardington Fire Tests [7] indicated that combinations of beam-web shear buckling and flange buckling are very prevalent under fire conditions. This phenomenon can significantly influence the internal forces in the connections. Flange buckling can raise the neutral axis, which changes the force distribution in the connection's components. Although at early stages of heating the top bolt rows would logically experience higher tensile force without flange buckling than when it has occurred, this situation may be reversed in the high-temperature catenary stage when, without a significant connection moment, most of the catenary force may be

carried by these rows. Local buckling at the beam ends will also have an effect on the deflection of the beam, and therefore influence the net tying force within the connection. The increased beam deflection during the heating phase of the fire will significantly increase the tension force on the connection during the cooling down period. However, the contribution of the combination of beam-web shear buckling and flange buckling in the vicinity of beam ends has not been taken into consideration by almost any of the existing research.

The behaviour of structural elements in real frames observed in the full-scale Cardington Fire Tests [2, 8-10] was very different from that observed in furnace tests on isolated elements. This indicates the importance of performance-based design, which sufficiently considers the interactions between various members of the structure. However, full-scale structural testing is expensive. To carry out finite-element modelling of an entire structure, including detailed representation of the connections, is computationally demanding, and is therefore not feasible for practical design. A practical alternative approach, component-based modelling of connections, has been proposed [11, 12].

The component-based method considers different parts of each connection as an assembly of individual nonlinear springs with predefined force-deformation characteristics. This method has been used to establish a connection element, which has been integrated into the software Vulcan [13], which was developed by the Structural Fire Engineering Research Group at the University of Sheffield. Vulcan is a three-dimensional program, allowing engineers to conduct three-dimensional structural robustness assessments. A variety of elements (beam-column,

connections, shear connector and slab) has already been implemented. Recently, Sun *et al*. [14, 15] developed a static-dynamic solution procedure for Vulcan. This procedure is able to capture re-stabilization after initial instability caused by local failure. For instance, this can be used to track the sequential failure of different connection components during progressive collapse of a whole structure. Sufficient validation [8, 9, 16-18] has been carried out to demonstrate that Vulcan is an accurate and computationally-efficient software to be used in performance-based fire engineering design.

Elghazouli et al. [19] implemented a local-buckling model within a frame analysis program to investigate the influence of local buckling at the beam ends on the fire response of frame members and sub-assemblies. This study indicated that, although local buckling at the beam ends may not directly trigger overall structural collapse, it can have detrimental effects on the deflections of, and load re-distributions between, structural elements. This will influence the fire resistance of the structure. However, the local buckling model presented in Elghazouli's work is based on elastic plate buckling theory, which is not appropriate for representing the buckling behaviour of Class 1 and 2 sections. No sufficient validation of the local-buckling model presented in his paper has been provided. A body of research [20-24] has been carried out to investigate the local in-plane flange buckling phenomenon, including both the pre- and post-buckling stages. Recent research has a common solution for the pre-buckling stage, while different collapse models [21-24] of the post-buckling stage have been proposed since 1965 [20]. The local buckling collapse mechanisms in all these models are composed of yield lines and plastic zones. The choices of possible

yield line patterns are based on experimental observations. All models assume that the yield lines, formed within the elastic buckling wavelength, will not change their positions in the post-buckling stage. However, these studies nearly all focus on the effects of local buckling on the rotational capacity and ductility of beam-ends, rather than on its influence on the global structural behaviour. Dharma extended the most up-to-date ambient temperature model, proposed by Gioncu and Petcu [24], to elevated-temperature applications for both steel beams [25] and composite beams [26] by introducing reduction factors to the flange buckling wavelengths to account for temperature-dependent material properties. In Dharma's research, the buckling wavelength is based on elastic plate buckling theory [27], in which the beam web acts as a rotational spring providing rotational restraint to the flange. However, this assumption tends to over-estimate the flange wavelength when the beam web is relatively thin (but may still be classified as Class 1 or 2 according to Eurocode 3 Part 1.1 [28]). Therefore, the results derived from Dharma's research have been shown to be extremely conservative for thin-web beams at elevated temperatures [29]. Moreover, Dharma's model considers beam-web buckling as a passive movement, which is caused by the rotation of the web-flange intersection when flange buckling occurs; the beam-web buckling wave is actually aligned vertically rather than diagonally, as would be the wave caused by shear force. However, a more obvious beam-web shear-buckle shape can be observed in the majority of images from the Cardington Tests, as shown in Fig. 1. This indicates that beam-web shear buckling is likely to be independent of flange buckling, and is triggered at least in part by shear force. The occurrence of shear buckling depends on various factors, such as the relative slenderness of the beam web and flanges and the relationship between

shear force and bending moment at the beam ends. The model also considers the consistency between the beam-web deflections caused by the two buckling modes.

Fig. 1. Flange buckling and beam-web shear buckling in combination [7].

This study proposes a new analytical model, which (1) considers the combination and interaction of flange buckling and web shear buckling; and (2) adopts a revised calculation approach for flange buckling wavelength to represent slender beams. This model has been compared with Dharma's model and finite element (FE) models using the ABAQUS software over a range of beam configurations and loading conditions. The FE models are initially short cantilevers in order to simulate the end buckling zone of a beam, intending to minimise the influence of deflection due to bending. The analytical model has been validated against these short-cantilever FE models. After validation, the analytical model has been implemented in calculating the deflection of a full-length beam, and this has been compared with an equivalent ABAQUS model. The analytical model will eventually be integrated into the software Vulcan, to be placed in structural models between the existing connection element, which is assumed to exist at the column-face, and the beam element, using a component-based approach. Performance-based analysis will then be carried out to investigate the overall structural behaviour under fire conditions.

2. Development of analytical model

The proposed analytical model uses a short cantilever to represent the beam-end buckling zone; the length of the cantilever, which is about to be equal to the beam depth d, is as shown in Fig. 2. By applying different combinations of moment and shear force at its free end, this model can represent the bucking panel at the end of a beam of any length, and with arbitrary loading and boundary conditions. Thus, it is possible to further implement this model as a buckling element into global frame analysis using Vulcan, as shown in Fig. 2. The corresponding shear force F and bending moment M at the end of the buckling element can be transferred from the adjacent part of the beam. This model aims to deal with the post-buckling phase when the full yield line mechanism has developed under certain loading conditions and temperatures. If these loading conditions cannot be fulfilled (for example when, for a simple beam, the bending moment is not large enough to trigger bottom-flange buckling), the proposed buckling element will remain a rigid body. The complete force-deflection relationship of the buckling element includes three stages: non-linear pre-buckling, plateau and post-buckling. If the material properties (Fig. 3) for steel at temperatures higher than 400°C are used, the vertical force-deflection relationship of the buckling element can be illustrated schematically as in Fig. 4.

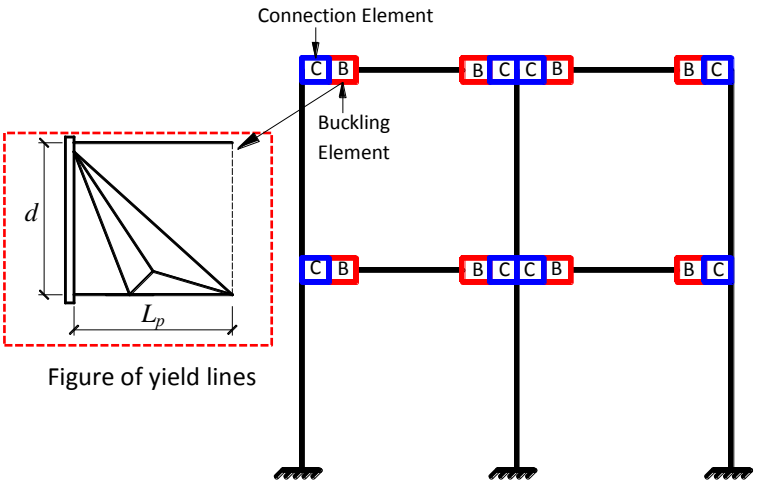

Fig. 2. Frame analysis including connections element and buckling element.

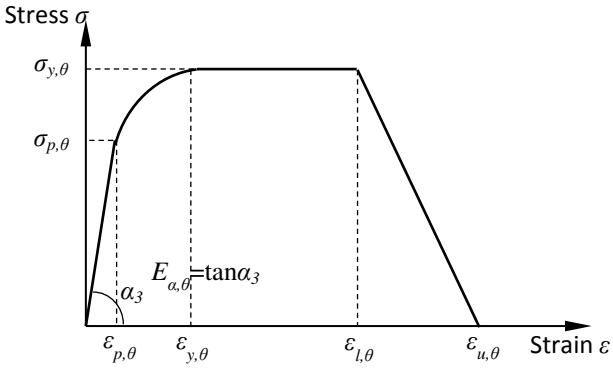

Fig. 3. Stress-strain relationship of structural steel.

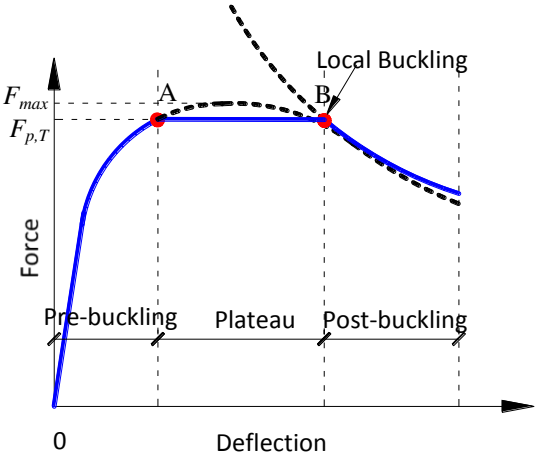

Fig. 4. Schematic force–deflection curve of a beam-end buckling model.

2.1 Pre-buckling stage

The characteristics of the buckling element in the pre-buckling stage are identical to those of the beam-column element [30] of Vulcan. The beam-column element is a three-noded line element with two Gaussian integration points along its length. Each of the three nodes has six degrees of freedom. The general segmented cross-section, which is capable of modelling different types of beam section, is shown in Fig. 5. The cross-section of the element is divided into a matrix of segments, each of which

allows consideration of its own material properties, temperature, stress and strain. The general continuum mechanics equations for large-displacement non-linear analysis are used to calculate the non-linear beam element matrix.

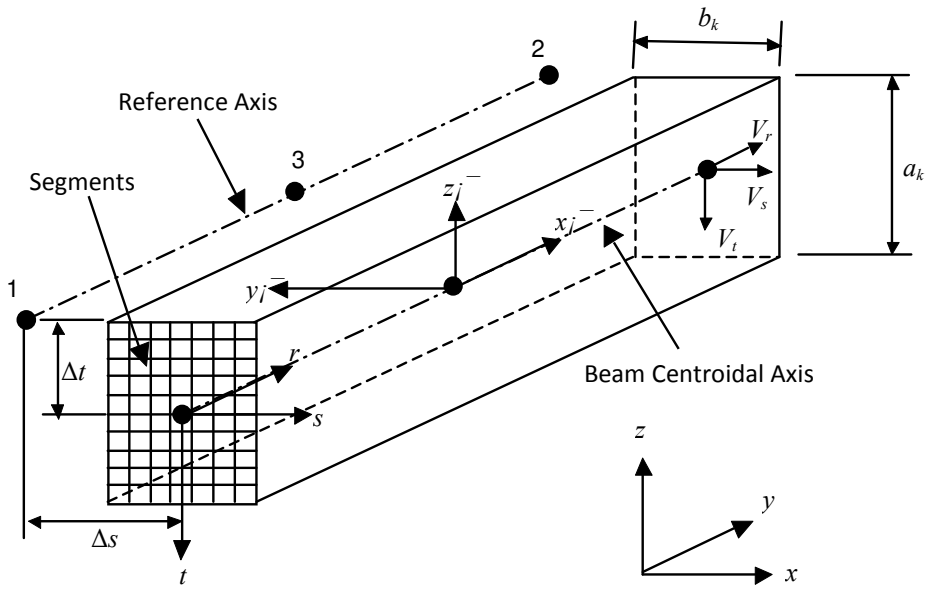

Fig. 5. Three dimensional segmented 3-noded beam-column element [30].

2.2 Plateau

The maximum flexural capacity F_{max}, as shown in Fig. 4, of an I-beam is generally less than 10% above the vertical force $F_{p,T}$, when the fully plastic moment resistance is reached at the middle of the flange buckling zone. This will be illustrated by the range of validation studies presented in Section 3.2, as well as some conducted by other researchers [25, 31]. This 10% discrepancy (the difference between F_{max} and $F_{p,T}$, as illustrated in (Fig. 4), can be regarded as a reserve of capacity. Therefore, it is reasonable to draw a plateau line at force level $F_{p,T}$ connecting Points A & B in Fig. 4 with the pre- and post-buckling curves; this has been defined as the plateau stage. This simplification will result in a reasonably conservative prediction.

2.3 Post-buckling stage

2.3.1 Development of plastic buckling mechanism

The plastic buckling mechanism (Fig. 6) forms at Point B in Fig. 4. The buckling mechanism is composed of yield lines and plastic yield zones. The yield line pattern adopted in this study is based on Dharma's model [29].

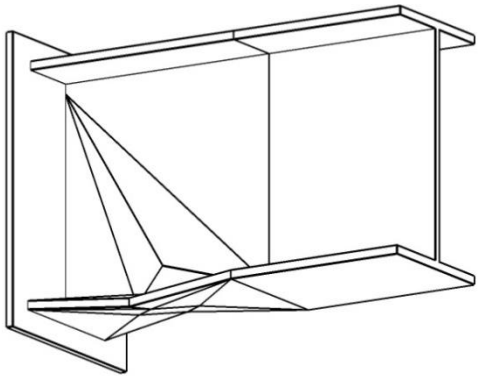

Fig. 6. Plastic Buckling Mechanism.

The deflection of the buckling zone is composed of the total deflection due to both bottom-flange buckling and beam-web shear buckling. In this study, the individual effects of these two buckling phenomena are considered. As the buckling zone is considerably shorter than the entire beam (as explained in detail in Beam-web shear buckling section), it is assumed that the influence of bottom-flange buckling is to cause a rotation of the whole beam-end about the intersection of the web yield lines, which is approximated as the top flange of the beam (due to stretching of the top flange and buckling of the bottom flange), as shown in Fig. 7(a). Beam-web shear buckling can cause transverse drift of the shear panel, as shown in Fig. 7(b).

Therefore, the combined effects of flange buckling and beam-web shear buckling on the overall beam vertical deflection is as expressed in Fig. 7(c).

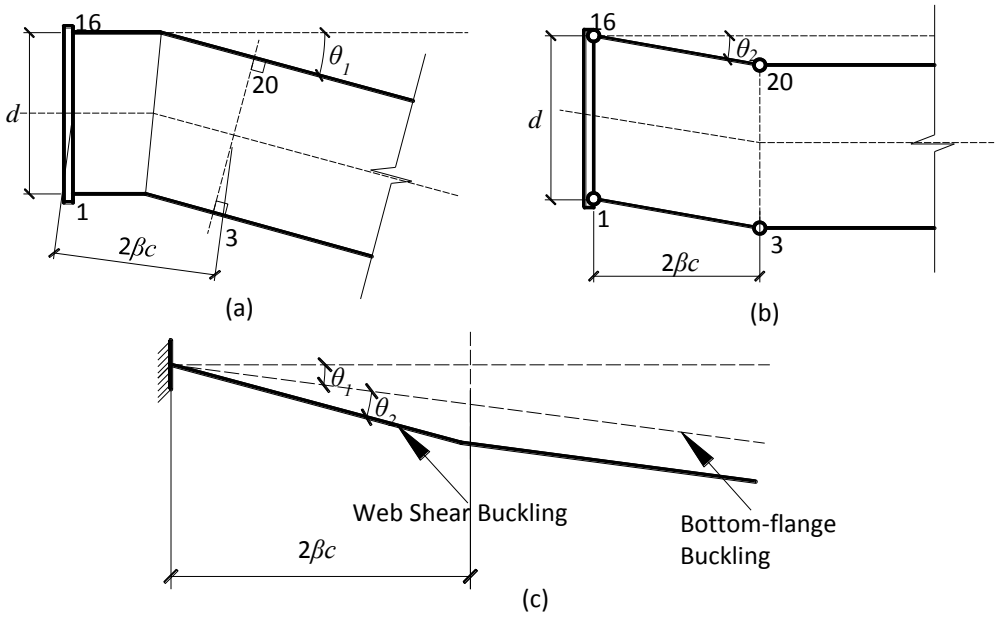

Fig. 7. The effects of flange buckling and beam-web shear buckling on beam vertical deflection (a) bottom-flange buckling; (b) shear buckling; (c) total deflection.

Bottom-Flange buckling

When bottom-flange buckling occurs, the buckled shape is composed of a squashed quadrilateral plastic zone (4-5-7-6) and several yield lines, as shown in Fig. 8(a). The centre of the plastic zone is at the centre of the buckled flange. It is assumed that the plate facets surrounded by the yield lines rotate rigidly about the yield lines. The plastic zone (shaded area in Fig. 8(a)) will be squashed along 5-6 due to compression; it can also rotate about Line 5-6. It is assumed that there is no relative rotation between the beam web and the bottom flange at their intersection (web and flange will always be perpendicular to each other). Therefore, the rotation of the plastic

zone in the bottom flange will lead to the rotation of the beam web, as shown in Fig. 9. This results in an isosceles-right-triangle plastic zone being formed in the beam web (5-6-11 in Fig. 10). This zone will be compressed along line 5-6 as well as rotate about this line. Several yield lines form in the beam web as a result of this rotation; the centre of rotation is located where the neutral axis of bending meets the beam end (Point 12 in Fig. 10). The angle of rotation due to bottom-flange buckling is θ_1, as shown in Fig. 7(c). The top flange remains in-plane, experiencing only plastic tensile deformation at the beam end, as shown in Fig. 8(b).

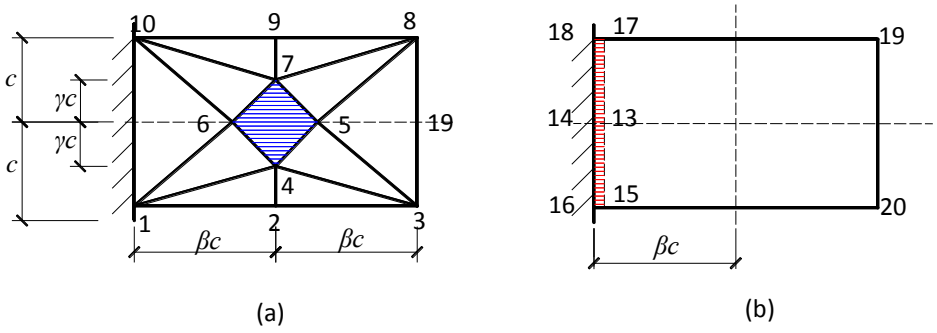

Fig. 8. Flange yield line mechanism (a) bottom flange; (b) top flange.

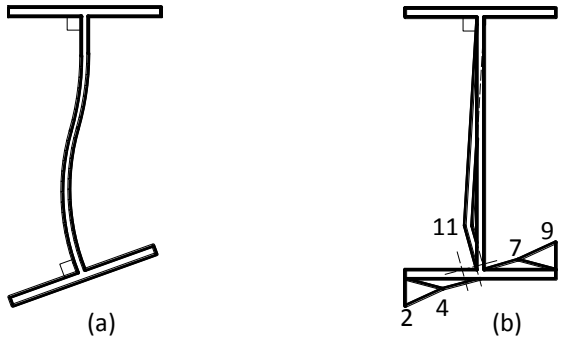

Fig. 9. Deformation compatibility between bottom flange and beam web (a) real-beam deformation; (b) deformation in the model.

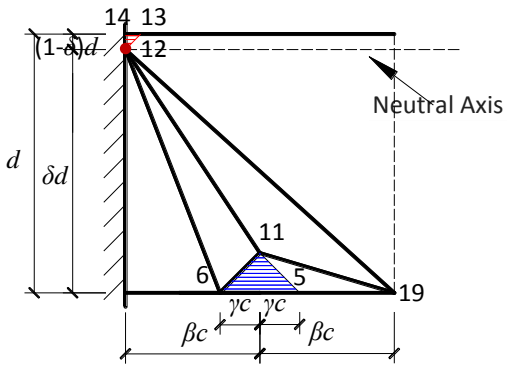

Fig. 10. Beam-web yield line pattern.

Beam-web shear buckling

When beam-web shear buckling occurs, the two opposite edges (Lines 1-16 and 3-20 in Fig. 7(b)) of the buckling panel move in parallel due to shear force, producing two plastic hinges on each of the top and bottom flanges. The angle of rotation due to this transverse drift is θ_2, as shown in Fig. 7(b). The four edges of the buckling zone are considered to be rigid. The beam web is assumed to be composed of tensile and compressive strips, which are aligned at 45° to the horizontal and perpendicular to each other, as shown in Fig. 11(a). When the buckling panel deforms due to shear force, the tensile strips are elongated due to the tensile force component of the vertical shear force, while the compressive stresses are shortened due to its orthogonal compressive force component. The out-of-plane deformation is assumed to occur only within the yield lines 12-6-19 (Fig. 10).

The out-of-plane deflection of the beam web due to bottom-flange buckling and that due to shear buckling need to be identical to ensure geometric compatibility. This

implies a relationship between the beam end rotations θ_1 and θ_2, due to bottom-flange buckling and shear buckling.

Length of the buckling panel

The flange-buckling wavelength given by Dharma [29] tends to considerably over-estimate the capacity of a slender beam. In most fire tests, only one shear-buckling wave has been observed, and the shear-buckling wave is usually aligned at around 45° to the horizontal. Therefore, the shear-buckling panel is usually no longer than the beam depth d, and the flange buckling wave lies in between the two plastic hinges in the bottom flange. Hence, the flange-buckling wavelength L_p can be calculated according to Eq. (1), considering the effects of steel grade and temperatures.

$$L_p = d\sqrt{275/\sigma_y}(k_E/0.7k_y) \quad (1)$$

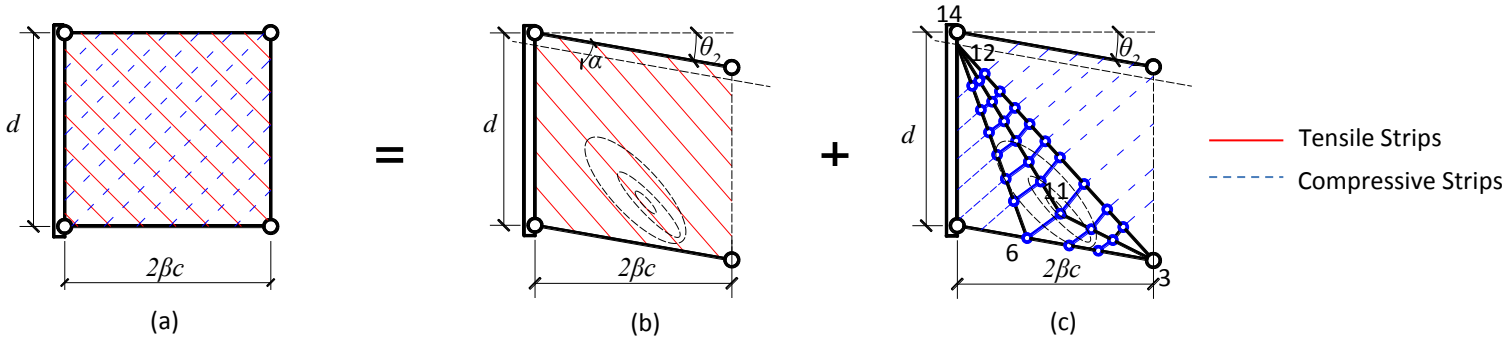

Fig. 11 Beam-web behaviour under shear force (a) Overall behaviour; (b) Tensile strips; (c) Compressive strips.

2.3.2 Calculation principle

The calculation principle is based on equality of the internal plastic work and the loss of potential energy due to the external load:

$$W_{\text{int}} = W_{ext} \tag{2}$$

Internal work

The internal plastic work W_{int} includes the work done in the flanges ($\sum_i (W_l)_i$ due to the rotation about the yield lines and $\sum_j (W_z)_j$ due to axial deformation of the plastic zones) and the work W_W done in the beam web due to its transverse drift during shear buckling. The deformations of the plastic zones are uniform across each of them, and the rotations about yield lines are uniform along every yield line. Summaries of the lengths and rotations of the yield lines, as well as the volumes and strains of the plastic zones, are given in Table 1 and 2. The total internal plastic work is then given by Eq.(3). The factor γ, which determines the dimension of the bottom-flange plastic zone, and the distance δd between the neutral axis of bending and the bottom flange, are determined through optimization on the basis of minimizing the total internal plastic work.

$$W_{\text{int}} = \sum_i (l_p t^2 \sigma_{y,\theta} \theta)_i / 4 + \sum_j (A_p t \sigma_{y,\theta} \varepsilon)_j + W_W \tag{3}$$

Table 1. Components of internal plastic work for plastic squash zones

Plastic Zones			
Zone(j)	Volume ($A_p t$)	Strain (ε)	Stress ($\sigma_{y,\theta}$)
4-5-7-6	$2\gamma^2 c^2 t_f$	$\theta_1 \delta d / (2\gamma c)$	$\sigma_{yf,\theta}$
5-6-11	$\gamma^2 c^2 t_w$	$\theta_1 \delta d / (2\gamma c)$	$\sigma_{yw,\theta}$
12-13-14	$(1-\delta)^2 d^2 t_w / 2$	θ_1	$\sigma_{yw,\theta}$
15-16-18-17	$2(1-\delta) c t_f d$	θ_1	$\sigma_{yf,\theta}$

Table 2. Components of internal plastic work for yield lines

Yeild Lines			
Line (i)	Length (l_p)	Rotation (θ)	Stress ($\sigma_{y,\theta}$)
2-4; 7-9	$(1-\gamma)c$	$2(\gamma / \beta\chi)^{1/2} \theta_1^{1/2}$	σ_{eq}
1-10; 3-8	$2c$	θ_2	σ_{eq}
1-4; 3-4; 7-8; 7-10;	$[\beta^2 + (1-\gamma^2)]^{1/2} c$	$\frac{1}{[\beta^2 + (1-\gamma^2)]^{1/2}} [\beta / (1-\gamma) + \frac{\beta^2 - 3\gamma - \gamma\beta + 1}{\gamma(1+\beta-\gamma)}] (\beta\gamma / \chi)^{1/2} \theta_1^{1/2} \sigma_{eq}$	
1-5; 3-6; 5-8; 6-10;	$[1 + (\beta-\gamma)^2]^{1/2} c$	$\frac{[1+(\beta-\gamma)^2]^{1/2}}{\gamma(1+\beta-\gamma)} (\beta\gamma / \chi)^{1/2} \theta_1^{1/2}$	σ_{eq}
4-5; 4-6; 5-7; 6-7;	$2^{1/2} \gamma c$	$2^{1/2} \frac{1}{\gamma(1+\beta-\gamma)} (\beta\gamma / \chi)^{1/2} \theta_1^{1/2}$	σ_{eq}
3-11	$((\gamma c)^2 + (\frac{1}{2} d)^2)^{1/2}$	$2^{1/2} [\frac{1-(1-\beta)\chi}{1-(1+\beta)\chi}]^{1/2} \theta_1^{1/2}$	$\sigma_{yw,\theta}$
6-11	$2^{1/2} \gamma c$	$(\frac{2}{\gamma})^{1/2} [\frac{1-(1+\beta/\gamma)\chi}{1-(1-\beta/\gamma)\chi}]^{1/2} \theta_1^{1/2}$	$\sigma_{yw,\theta}$
5-12	$[1 + (1+\beta)^2 \chi^2]^{1/2} \delta d$	$\frac{1}{\chi^{1/2}} [\frac{1-(1-\beta)\chi}{1-(1+\beta)\chi}]^{1/2} [1 + (1+\beta)^2 \chi^2]^{1/2} \theta_1^{1/2}$	$\sigma_{yw,\theta}$
6-12	$[1 + (1-\beta)^2 \chi^2]^{1/2} \delta d$	$\frac{1}{\chi^{1/2}} [\frac{1-(1+\beta/\gamma)\chi}{1-(1-\beta/\gamma)\chi}]^{1/2} [1 + (1-\beta/\gamma)^2 \chi^2]^{1/2} \theta_1^{1/2}$	$\sigma_{yw,\theta}$
11-12	$[(1-\chi)^2 + (\beta\chi/\gamma)^2]^{1/2} \delta d$	$[\frac{(1-\chi)^2 + (\beta\chi/\gamma)^2}{(1-\chi)^2 - (\beta\chi/\gamma)^2}]^{1/2} \theta_1^{1/2}$	$\sigma_{yw,\theta}$
15-13-17	$2c$	$[\frac{(1-\chi)^2 + (\beta\chi/\gamma)^2}{(1-\chi)^2 - (\beta\chi/\gamma)^2}]^{1/2} \theta_1^{1/2}$	σ_{eq}
16-18; 19-20	$2c$	θ_2	σ_{eq}

In Table 2, $\chi = (\gamma c) / (\delta d)$. The flexural capacity of each yield line on the flanges can be represented as Eq. (4).

$$M_{eq} = b_f t_f^2 \sigma_{eq} / 4 \tag{4}$$

The normal stresses σ_r, which are perpendicular to the yield lines, and the shear stresses τ_r which are parallel to the yield lines (Fig. 12) can both influence the reduced yield stresses σ_{eq} across the yield lines, and therefore cause a reduction of the flexural capacity M_{eq}. The stresses σ_r and τ_r are components of the axial stresses σ_{tf} and σ_{cf}, parallel to the beam length, which are caused by overall beam bending. According to the Mohr's Circle in Fig. 12, σ_r and τ_r can respectively be calculated using Eq. (5) and (6).

$$\sigma_r = 0.5(1+\cos(2\alpha_1))\sigma_{t(c)f} \tag{5}$$

$$\tau_r = 0.5\sin(2\alpha_1)\sigma_{t(c)f} \tag{6}$$

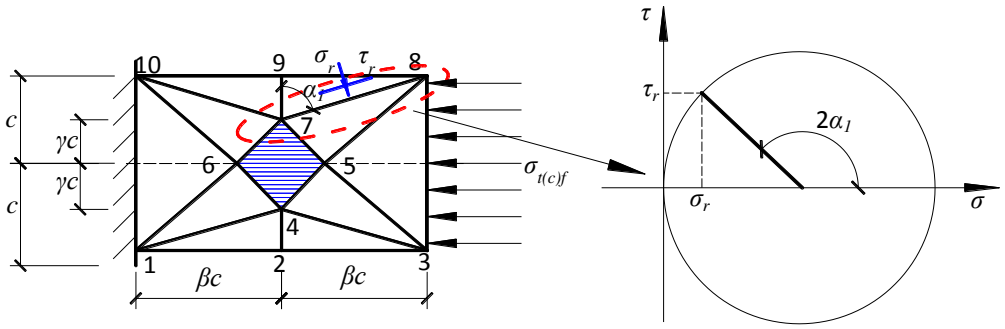

Fig. 12. Mohr's circle for one yield line (7-8).

in which α_1 is the acute angle between the yield line and the vertical axis. The yield stress σ_{eq1} of the yield lines, considering only the effect of σ_r, is given as Eq.(7).

$$\sigma_{eq1} = \sigma_{yf,\theta}[1-(\sigma_{t(c)f} / \sigma_{yf,\theta})^2] = \sigma_{yf,\theta}[1-(\frac{(0.5(1+\cos(2\alpha_1))\sigma_{t(c)f}}{\sigma_{yf,\theta}})^2] \quad (7)$$

The relationship between the shear stress τ_r and the reduced equivalent yield stress σ_{eq} can be expressed as Eq. (8).

$$(\sigma_{eq} / \sigma_{eq1})^2 + (\tau_r / \tau_{eq1})^2 = 1 \quad (8)$$

where $\tau_{eq1} = \sigma_{eq1} / \sqrt{3}$.

Substituting Eq. (7) into Eq. (8) gives

$$\sigma_{eq} = \sigma_{yf,\theta}[1-(\frac{0.5(1+\cos(2\alpha_1))\sigma_{t(c)f}}{\sigma_{yf,\theta}})^2][1-(\frac{0.5\sin(2\alpha_1)}{\sqrt{3}})^2]^{1/2} \quad (9)$$

It has previously been ascertained [32] that the internal work of the deformed beam web due to shear buckling is given by:

$$W_W = W_T + W_C = \frac{d\sigma_t t\cos(\alpha+\theta_2)\sin\alpha}{\cos\theta_2}\Delta_{vs} + \frac{d\sigma_c t\sin(\alpha+\theta_2)\cos\alpha}{\cos\theta_2}\Delta_{vs} \quad (10)$$

where α is the angle between the tensile strips and the upper edge of the shear-buckling panel, as shown in Fig. 12 (b). Δ_{vs} is the vertical displacement of the shear-panel edge, which is equal to $2\beta c\theta_2$. According to the Huber-von Mises plasticity criterion [33], the relationship between the tensile and compressive stresses for a two-dimensional panel is given by

$$\sigma_c^2 + \sigma_t^2 + (\sigma_t - \sigma_c)^2 = 2\sigma_{yw,\theta}^2 \quad (11)$$

The compressive strips in the beam web can be regarded as struts, each of which has three plastic hinges, as shown in Fig. 13. It is assumed that the central plastic hinge always forms at the mid-length of each strut, although this assumption may result in a shear buckle shape which is slightly different from reality. For each strut, the rectangular cross section can be divided into two parts (Fig. 14). The axial compressive stress of the strut is resisted by Region A while its bending moment is resisted by Region B. Therefore,

$$P_c = \sigma_c h_c f \quad (12)$$

$$M_p = f(t_w^2 - h_c^2)\sigma_c / 4 \quad (13)$$

The force equilibrium between the compressive resistance P_c and the plastic moment resistance M_p of the plastic hinge is

$$P_c \Delta_1 = 2M_p \quad (14)$$

Substituting Equations (12) and (13) into Eq. (14), the height h_c of Zone A, resisting compression, can be calculated. Assuming that the compressive stress within Zone A remains at yield, the overall resistance of the strut is proportional to h_c. Therefore, the average compressive stress σ_c of the strut is also proportional to h_c, which gives

$$\sigma_c = h_c \sigma_{yw,\theta} / t_w \quad (15)$$

Substituting Eq. (15) into Eq. (11) gives the tensile stress σ_t and the compressive stress σ_c in each strip. Therefore, according to Eq. (10), the internal plastic work W_W caused by shear buckling of the beam web can be calculated.

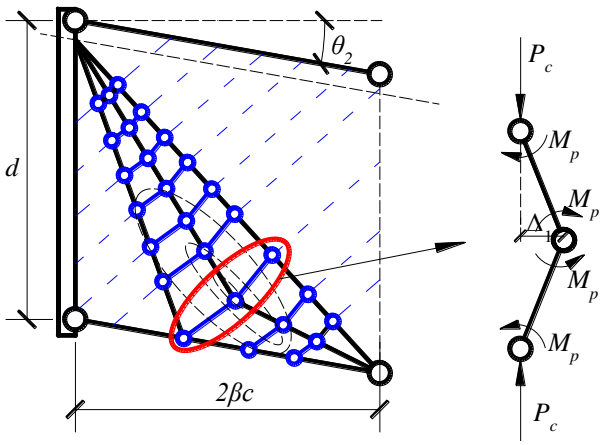

Fig. 13. Strut representing an arbitrary compressive strip.

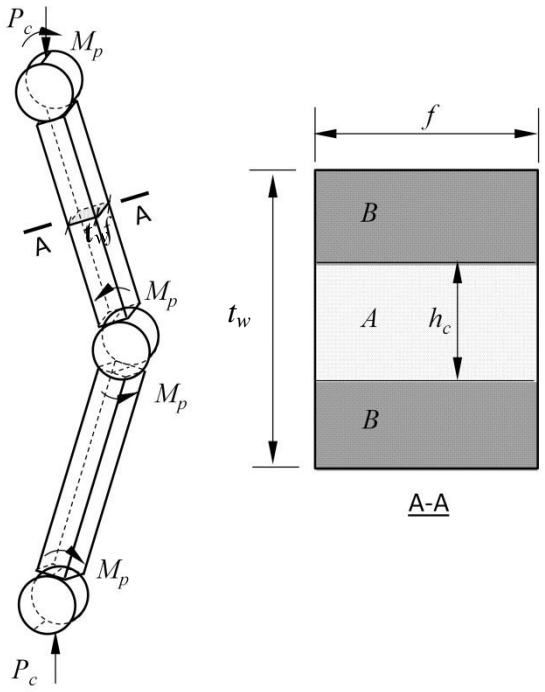

Fig. 14. Cross section of one strut [32].

External work

The total external work can be expressed by Eq. (16), where Δ_i includes the deflections caused by both bottom-flange buckling and beam-web shear buckling. Elastic deflection can be neglected due to the relatively short length of the buckling element.

$$W_{ext} = \sum P_i \Delta_i = F(4\beta c)\theta_1 + F(2\beta c)\theta_2 + M((4\beta c)\theta_1 + (2\beta c)\theta_2)/(4\beta c) \quad (16)$$

Deflection compatibility

The deflection compatibility is based on the assumption that the out-of-plane deflection of Point 11 (Fig. 16) caused by bottom-flange buckling is identical to that caused by shear buckling.

For the out-plane deflection caused by bottom-flange buckling, the side lengths of the Triangle 1-4-5, shown in Fig. 15, are illustrated in Eq. (17) - (19):

$$l_1 = [1 + (\beta - \gamma)^2]^{1/2} c \quad (17)$$

$$l_2 = 2^{1/2} \gamma c \quad (18)$$

$$l_3 = [\beta^2 + (1 - \gamma)^2]^{1/2} c \quad (19)$$

The angle of rotation of Line 1-5 is

$$\theta = \frac{[1+(\beta-\gamma)^2]^{1/2}}{\gamma(1+\beta-\gamma)}(\beta\gamma/\chi)^{1/2}\theta_1^{1/2} \tag{20}$$

According to the geometry, the out-of-plane deflection of Point 4 (Fig. 15) is

$$h_1 = l_{4-100}\sin(\theta) = \sin(\theta)\times\sqrt{l_2^2-(\frac{l_2^2+l_3^2-l_1^2}{2l_3})^2} \tag{21}$$

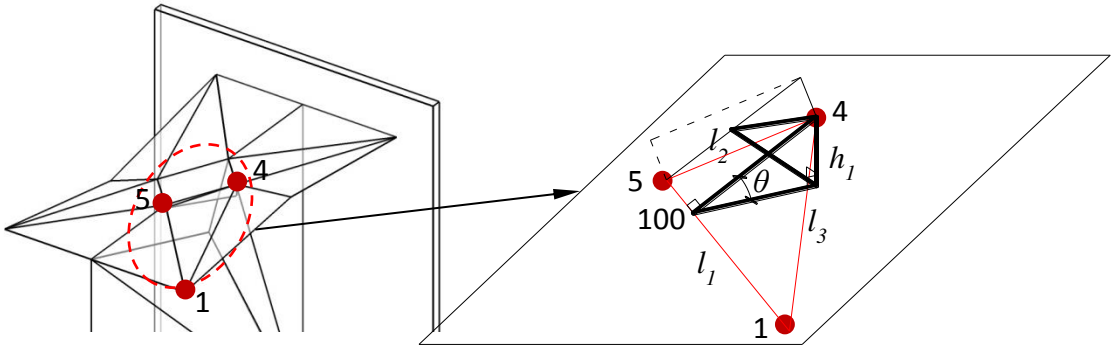

Fig. 15. Deformed shape caused by bottom-flange buckling.

The out-of-plane deflection of Point 11 (Fig. 6(a)) on the beam web, caused by bottom-flange buckling, is equal to h_1.

For the out-of-plane deflection caused by shear buckling, the initial length (as shown in Fig. 16 (a)) of the compressive strut, which contains Point 11, is

$$l_4 = \frac{\beta+\gamma}{2\beta}\times\sqrt{2}d \tag{22}$$

The deformed length of the same compressive strut is

$$l_5 = 2 \times \frac{\beta + \gamma}{2\beta} \times d \sin(\pi / 4 - \theta_2 / 2) \tag{23}$$

The side lengths of the triangle, as shown in Fig. 16 (b), are

$$x_2 = \sqrt{2}\gamma c \tag{24}$$

$$x_3 = l_4 - l_5 / 2 - x_2 \tag{25}$$

$$x_4 + x_5 = l_5 / 2 \tag{26}$$

According to the geometry, h_2 can be calculated as

$$h_2 = \sqrt{(x_3)^2 - (\frac{x_3^2 - x_2^2 + (l_5 / 2)^2}{l_5})^2} \tag{27}$$

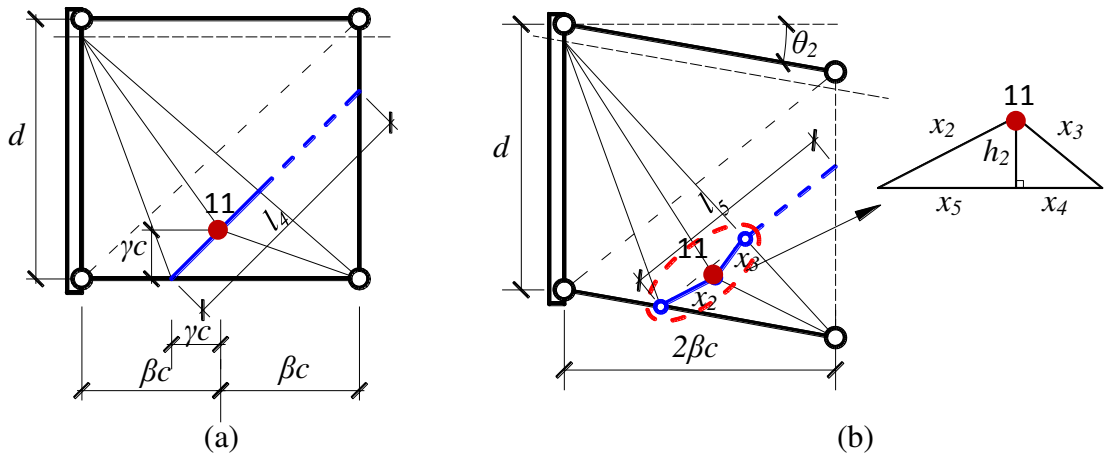

Fig. 16. Deformed shape caused by shear buckling of the beam web.

3. Validation against finite element modelling

3.1 Validation of FE model against experimental results

The finite element software ABAQUS has been used to develop the finite element modelling. In this section, the FE models are validated against the experimental results published by Dharma [31].

Experimental programme

Dharma [31] tested nine steel I-beams up to failure. In this paper four out of the nine I-beams have been chosen to validate the numerical models. All four I-beams failed by local bottom-flange buckling. To validate the FE model at the post-buckling stage, the specimens which demonstrated clear descending force-displacement relationships after the occurrence of local buckling have been selected. The test numbers for the four beam sections are S3-2, S3-3, S4-1 and S4-2. The test setup is shown in Fig. 17. There is one stiffener at each end of the beam, as well as one at mid-span. No axial restraint was applied during the testing, so that no axial force was caused by thermal expansion. The specimens were heated to constant temperature before the hydraulic jack applied a static point load at the mid-span.

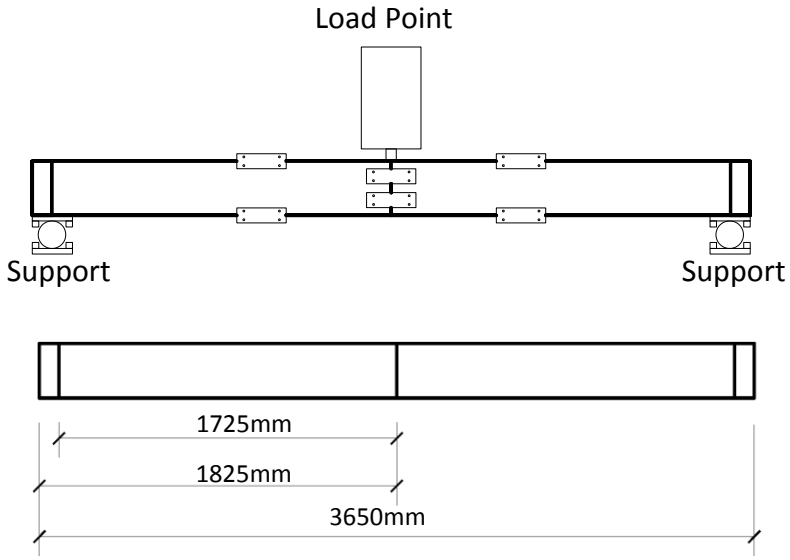

Fig. 17. Test set-up [26].

The results of the tensile coupon tests on these specimens at ambient temperature are given in Table 3.

Table 3. Results of tensile coupon tests at ambient temperature (MPa)

Beam No.		Yield Stress	Elastic Modulus	Ultimate Strength
S3-2	flange	224.1	201697	392.1
	web	277.1	206063	452.0
S3-3	flange	224.1	201697	392.1
	web	277.1	206063	452.0
S4-1	flange	393.5	205283	545.1
	web	449.4	205700	590.3
S4-2	flange	393.5	205283	545.1
	web	449.4	205700	590.3

These tests were used to validate the ABAQUS models, although the test setup was not identical to the exact conditions (restraint to thermal expansion, boundary conditions and the ratio of shear to moment in the buckling panel), which a real beam would experience in a real fire. The validated FE models, subject to more realistic conditions, were then used to verify the analytical model.

Numerical modelling

In this study, the four-noded shell element (S4R) of ABAQUS, which is capable of simulating buckling behaviour with reasonable accuracy, was adopted. A mesh sensitivity analysis was conducted, which indicated that elements of size 15mm x 15mm provided an optimum between accuracy and computing efficiency. Arc-length analysis [34] was carried out to track the descending load path of the buckling zone at the post-buckling stage. The shape of the initial imperfection was based on the first buckling mode. A small amplitude $(d+t_f)/100$ was adopted in order to trigger the asymmetric bottom-flange buckling mode without unduly influencing the load capacity of the buckling zone. Regarding the material properties used in the numerical modelling, the ambient-temperature coupon test results, as shown in Table. 3, were reduced by applying the reduction factors for proportional limit stress, yield stress and Young's modulus, as given in BS EN 1993-1-2. The finite element model is illustrated in Fig. 18. As the end supports were directly below the stiffeners, only the length of the beam between the two end stiffeners was modelled. The length of the model was 3450mm. Multi-Point Constraints (MPC) [34] which allow constraint of the motion of slave nodes of a region to the motion of a point, were applied in ABAQUS between Points 1 and the left-end stiffener, as well as between Point 2 and the right-end stiffener. Boundary conditions were then applied to Points 1 and 2. For Point 1, all six degrees of freedom (DoF) were restrained except for rotation about the x-axis, whereas Point 2 was free to rotate about x and to move in translation parallel to z with the other DoFs constrained. In other words, the two beam ends could both rotate about x, and there was no restraint to thermal

expansion of the beam. MPC make it convenient to model pin-ended beams. A point load was applied to the mid-span of the beam. Table 4 presents the details of cross-section dimensions and test temperatures. All dimensions are the average values of measurements by Dharma [26] from different locations.

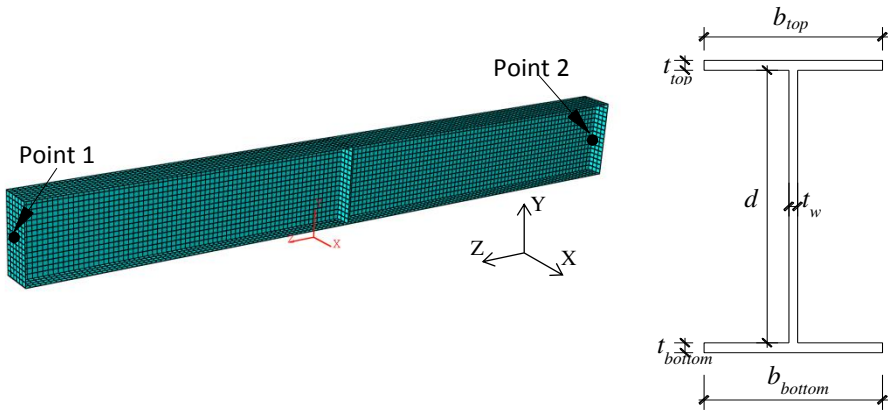

Fig. 18. Finite element model. (a) Image of finite element model; (b) cross section dimensions (in mm).

Table 4. Measured cross-section dimensions (in mm) and test temperature (in °C)

Test No.	b_{top}	b_{bottom}	t_{top}	t_{bottom}	d	t_w	T
S3-2	162.89	163.51	10.00	9.95	275.5	8.14	415
S3-3	162.72	164.00	10.30	10.19	275.93	7.95	615
S4-1	176.70	178.26	10.08	10.46	380.76	7.83	415
S4-2	177.83	176.71	10.29	10.52	380.78	7.76	615

A comparison between the FE modelling and experimental results is shown in Fig. 19. The lines represent the FE results while the data points represent test results. Good agreement between the test and the FE modelling results was obtained, except for S4-1, in which the FE model predicts lower capacity than that measured during testing. Since all the other three groups indicate good reliability of the FE models, the failure load given by Test S4-2 (same specimen as in Test S4-1, but tested at 615°C) was used to predict the failure load of Test S4-1 (at 415 °C), using the

strength reduction factors given in EC3 [35]. This calculated failure load agrees with the modelling result. It is possible that the loading rate applied in Test S4-1 may have been too fast, resulting in an increase of the failure load, as has been experienced in other studies [36]. The discrepancy between Test S3-2 and FEA S3-2 in the deflection range of 10 mm to 80 mm is possibly caused by the discrepancy between the real high-temperature mechanical properties of the tested steel and the properties used in the modelling (ambient-temperature coupon test results with the EC3 reduction factors applied). The FE models can also predict well the buckling shape compared with the test results; one example is shown in Fig. 20. Therefore, the numerical model is considered reliable and is used in the following study.

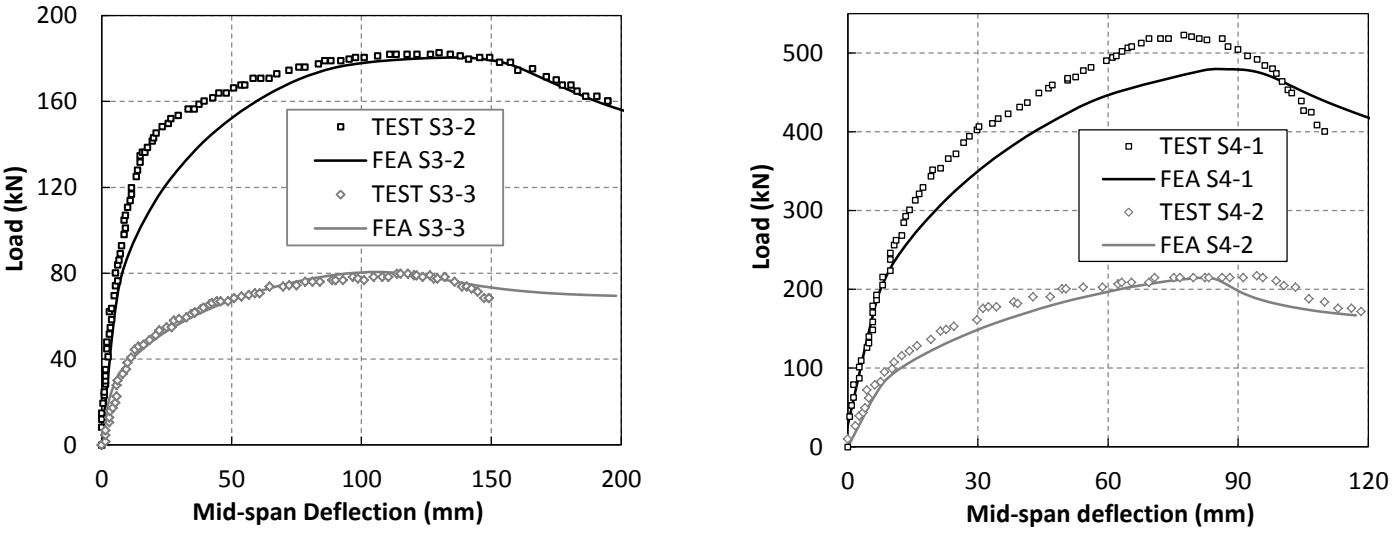

Fig. 19. Load-deflection comparison between FEA and test results.

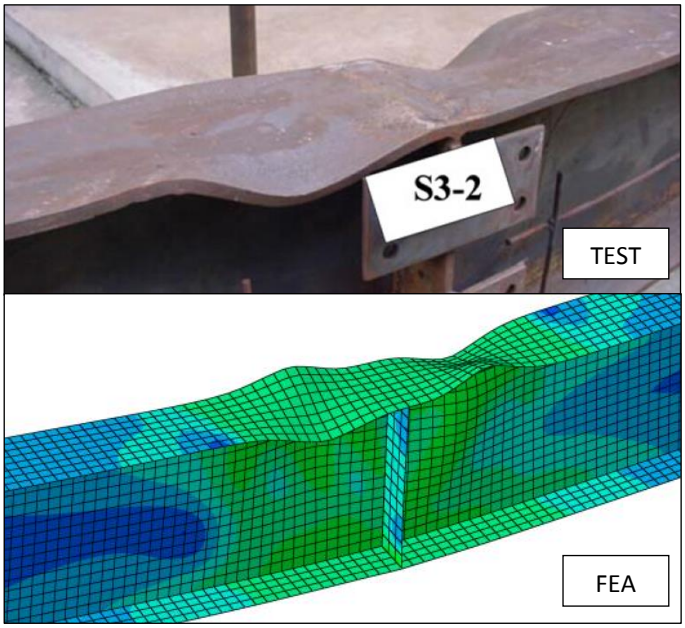

Fig. 20. Comparison of failure modes of Test 3-2 [26] and FEA.

3.2 Comparison between the analytical model, Dharma's model and FEA

After validation, 48 FE models (Table 5), of various beam configurations and loading conditions were analysed at different temperatures. An illustration of an FE model, and its loading and boundary conditions, is shown in Fig. 21. A short cantilever with the length/depth ratio equals to 2 was modelled. This length/depth ratio is chosen to ensure that (1) the model will include at least one full buckling wavelength, and (2) the effects of the boundary conditions can be minimised. The flexural curvature of this short beam-end buckling zone can be neglected. Different combinations of shear force and bending moment were applied, as shown in Table 4.

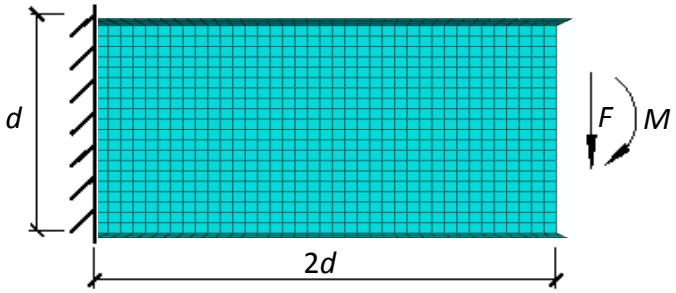

Fig. 21. The finite element model

These cases have been divided into two groups, FEA1 and FEA2. The models in FEA1 are of the same dimensions as the specimen of Test S3-2 (Table 4), with web thicknesses varying between different models. Similarly, FEA2 uses the Test S4-2 specimen dimensions, again with different web thicknesses. Since this research focuses on Class 1 and 2 beams, the variation of web thicknesses is limited within this range. Temperatures of 415°C and 615°C have been applied. The material properties of the flanges of the test specimens S3-2 and S4-2 have been used for FEA1 and FEA2 models, respectively.

Table 5. Detailed group information

	Web thickness	Moment-shear force ratio M/F (in mm)	Temperatures (°C)	
FEA1	5mm	500 1000 1500	415	615
	6mm	500 1000 1500	415	615
	7mm	500 1000 1500	415	615
	8mm	500 1000 1500	415	615
FEA2	5mm	500 1000 1500	415	615
	6mm	500 1000 1500	415	615
	7mm	500 1000 1500	415	615
	8mm	500 1000 1500	415	615

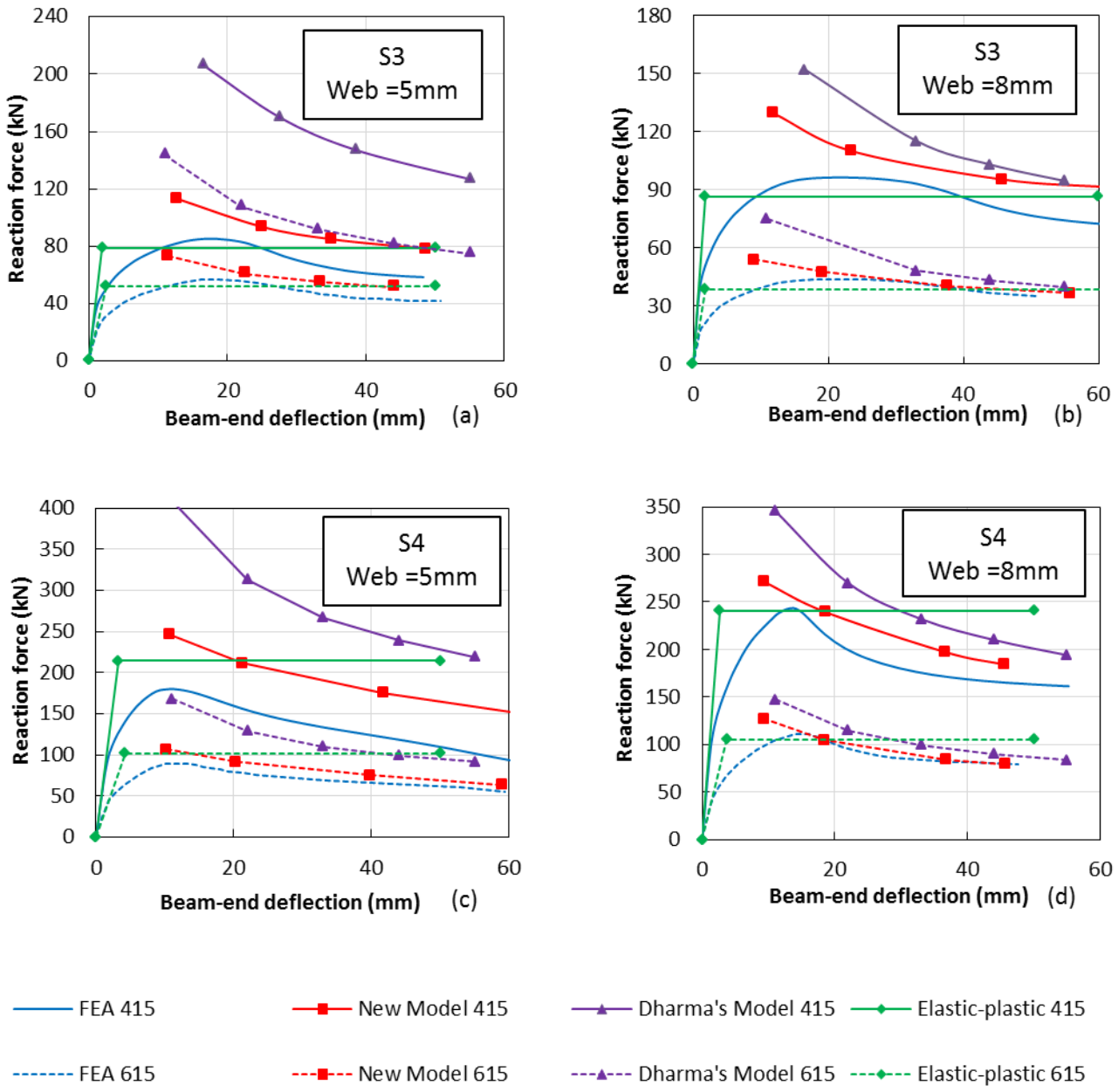

Fig. 22. Comparison between the analytical model, Dharma's model and FE analysis

The force-displacement relationships given by the proposed analytical model, Dharma's model and the ABAQUS analyses have been compared. Fig. 22 shows the comparisons for the two models with the largest and smallest web thicknesses (5mm and 8mm) subject to bending and shear force at M/F = 1000mm. Each part of Fig. 22 includes eight curves, representing the comparison between the analytical model, Dharma's model, FE analysis and the elastic-plastic curve (with peak loads assessed by assuming plastic moment resistance is reached at the middle of the flange buckling zone) at two different temperatures. The proposed analytical model gives upper-bound results compared to the FE models for all cases; it also gives more accurate results than that of the Dharma's model in all cases. The results from Fig. 22 show that the maximum flexural capacity $\mathrm{F_{max}}$ of an I-beam is generally less than 10% above the vertical force $\mathrm{F_{p,T}}$. The analytical model captures results for beams at 615°C better than at 415°C. This may be because the accuracy of the assumption of flange buckling length from Eq. (1) may differ at different temperatures; this would have a significant effect on the beam post-buckling behaviour. Fig. 23 shows a comparison of the force-web-thickness relationships between the new model and Dharma's model. The variable F_{FEA} represents the peak load given by the FE modelling. F_N and F_D respectively represent the load level of the new analytical model and that of Dharma's model, at the deflection at which the FEA model reaches its peak load. The vertical axis of Fig. 23 represents F_N and F_D normalized with respect to the corresponding F_{FEA}. As shown in this figure, Dharma's model tends to overestimate the beam loading capacity when the web is thinner (of 5mm or 6mm thickness), whereas it gives a good prediction at larger web thicknesses (7mm and 8mm). The new analytical model is able to give a better upper bound of

the beam load capacity for both slender and stocky beams within the analysed range. The proposed analytical model has been designed for Class 1 and 2 beams, whereas the two models of web thicknesses 5mm and 6mm in FEA2 fall into the Class 3 range. This explains the reason for the larger discrepancy between the proposed model and the FEA for these two cases. It is, therefore, indicated that the new model gives a reasonable prediction of the load capacity of the beam end buckling zones of Class 1 and 2 beams at the post-buckling stage.

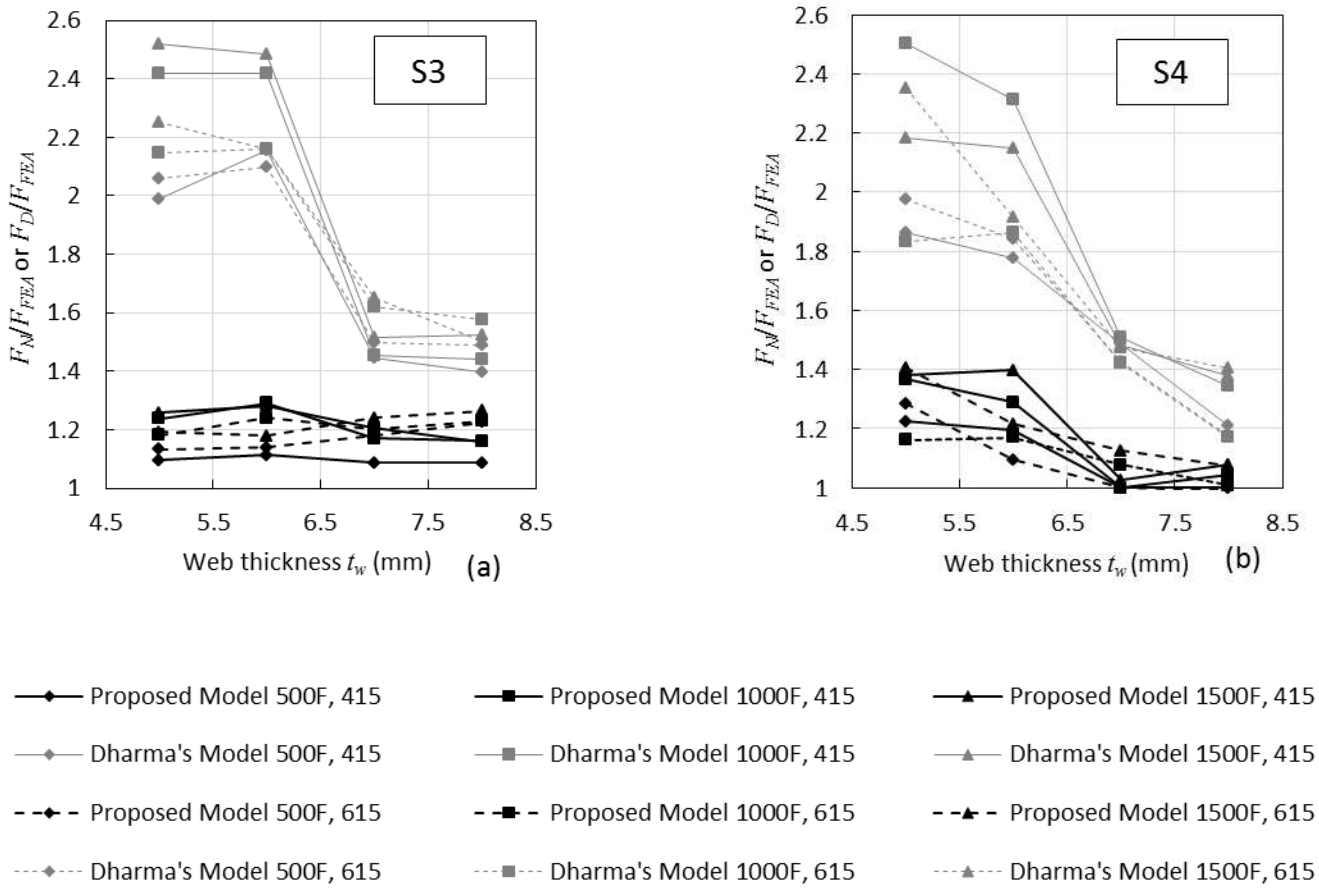

Fig. 23. Comparison of predictions of the new model and Dharma's model: (a) FEA1; (b) FEA2.

3.3. Integration into a full beam model

In this section, the validated beam-end model, as described in Section 3.2, has been integrated into a whole beam. A calculation example is given below.

In this example, the beam-end model of 8mm web thickness in Group FEA1 is selected and integrated into the full beam model. The length of the beam model is 5m, given that a beam depth to length ratio of 1/20 is commonly used in design practice. A vertical point load is applied at the mid-span of the beam. The beam is fully fixed against rotation at both ends, with one end being free to move axially to allow thermal expansion. The beam is heated to to 615°C, the same as for the corresponding beam-end model. One half of the beam is modelled in ABAQUS, using symmetry boundary conditions. The contours of out-of-plane deflection are shown in Fig. 24(a). The deformed shape is shown in Fig. 24(b). For this loading condition, the hogging moment at the beam end is identical to the sagging moment at the mid-span. Therefore, top-flange buckling at the mid-span occurs simultaneously with bottom-flange buckling at the beam end. Beam-web buckling occurs at both the beam end and mid-span. The mid-span deflection (Δd) consists of twice the sum of (1) the deflection Δd_1 due to the beam-end rotation caused by bottom-flange buckling, (2) the transverse drift Δd_2 due to shear buckling and (3) the deflection Δd_3 due to normal bending curvature of one quarter of the beam. The force-deflection relationships given by the FEA and the analytical models are shown in Fig. 25. The curve with triangular markers plots the results given by the analytical model which was developed to simulate the post-buckling behaviour, and the dashed line represents the FE results. The comparison shows that the proposed analytical model

provides reasonably accurate and upper-bound results for a whole beam. The pre-buckling elastic and plastic stages can be reproduced accurately by Vulcan, using its existing beam element as introduced in Section 2.1. The horizontal plateau is achieved as described in Section 2.2. Therefore, the thick line indicates the whole force-deflection relationship of the example beam with buckling zones, covering all three stages.

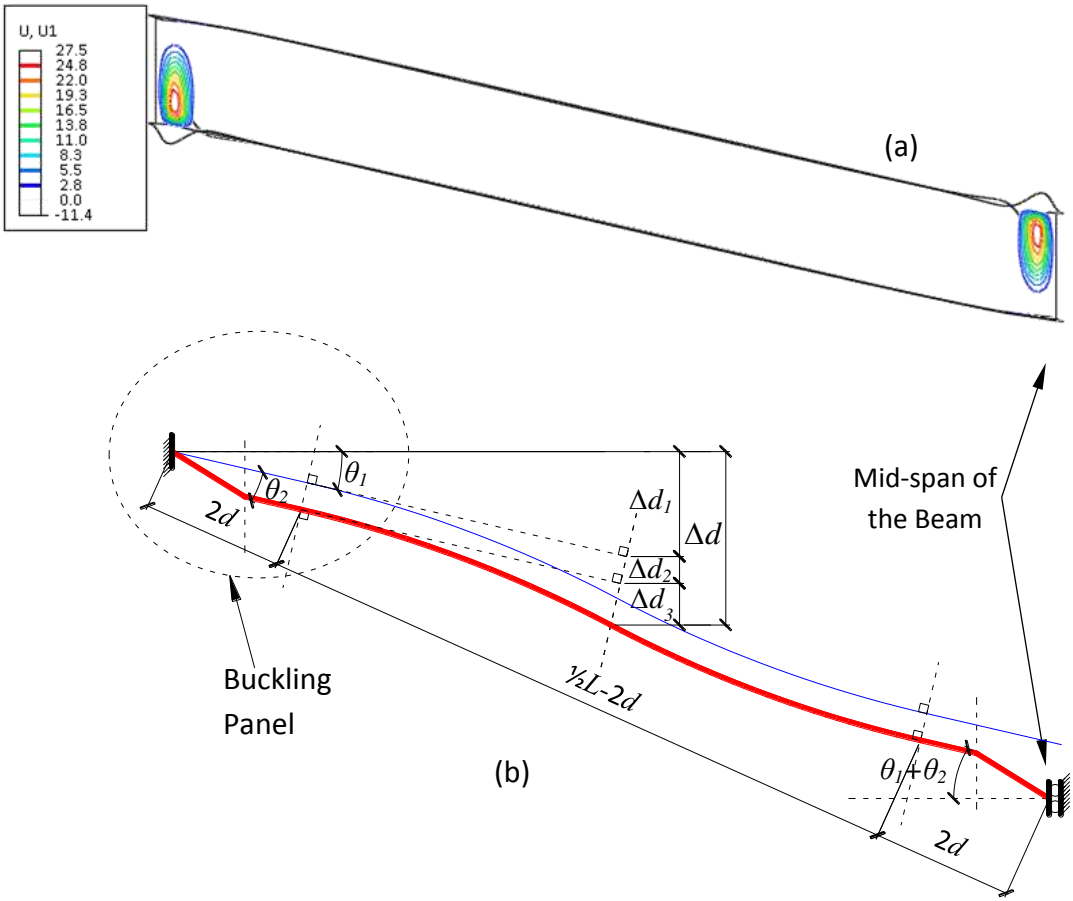

Fig. 24. Deformed shape: (a) ABAQUS contour; (b) Simplified theoretical deformed shape.

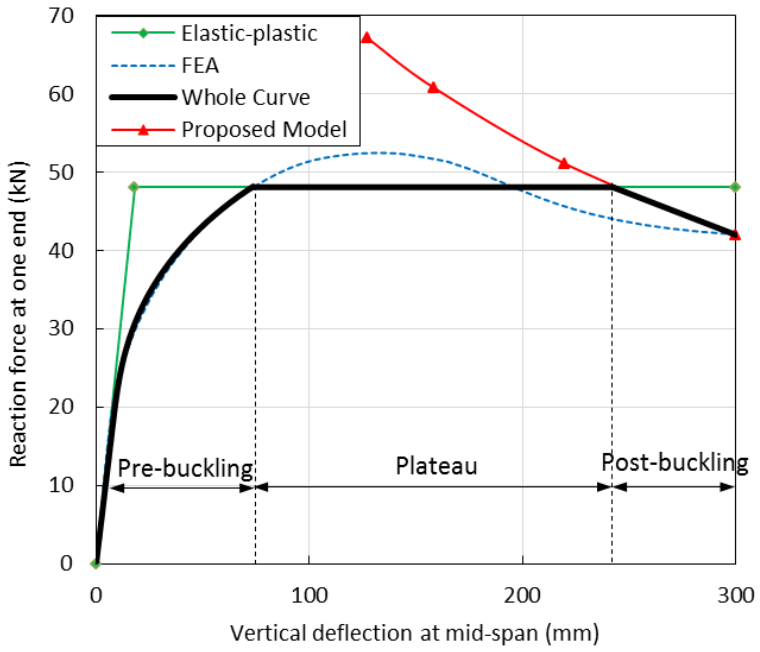

Fig. 25. Force-deflection relationship of the example beam.

4. Component-based model

One of the major objectives of this research is to develop a component-based beam-end buckling element, consisting of two components representing web shear buckling and bottom-flange buckling, respectively. This element will then be embedded into Vulcan to carry out global performance-based structural fire engineering analysis.

The component-based method divides the beam-to-column connections and the adjacent buckling panels into components. The characteristics of each component can be described as those of a nonlinear spring. The overall behaviour of the connection can be achieved by assembling these springs. When carrying out the analysis, the column-side boundary of the buckling element is fully fixed in order to isolate it from the connection element. The buckling and connection elements can individually deal with their own displacements and rotations. The deflections of the

two can be superposed in the global analysis. The buckling element can be connected to any kind of connection element, including pinned, semi-rigid and rigid elements. Whether the buckling element will experience buckling depends on the loading and heating conditions, and the configuration of the analysed structure.

A body of research [6, 11, 12] on different types of connection components has already been carried out. The new flange-buckling component has been connected directly to the existing connection element; the new beam web-shear buckling element is then connected between this and the beam element, as shown in Fig. 26. In this figure, the region named “Connection element” represents Region C in Fig. 2, which is the existing beam-to-column connection element. The region named “Buckling element” represents Region B in Fig. 2, which is the beam-end buckling element. The bottom-flange buckling component, representing the beam-end buckling element is a compressive spring to simulate the rotation of the beam end due to bottom-flange buckling. It is assumed that its centre of rotation is at the top of the cross section, on the basis of the analytical model. The stiffness of the compressive spring is infinite before buckling occurs, and is given by Eq. (28) for the post-buckling stage:

$$k_1 \Delta L_2 d = M \ , \ k_1 = M / (d^2 \theta_1) \tag{28}$$

The length of the shear buckling component is non-zero, since the transverse drift of the beam end due to shear buckling is affected by the length of the shear panel. The length (L_3) of the beam-web shear buckling component has been defined to be identical to beam depth (d) to be consistent with the analytical model and also to

simplify the model setup process in Vulcan. The stiffness of the compressive spring before bottom-flange buckling is infinite, while that in the post-buckling stage is given by Eq. (29):

$$k_2 \frac{1}{2} d\theta_2 = F \,,\; k_2 = 2F / (d^2 \theta_2) \tag{29}$$

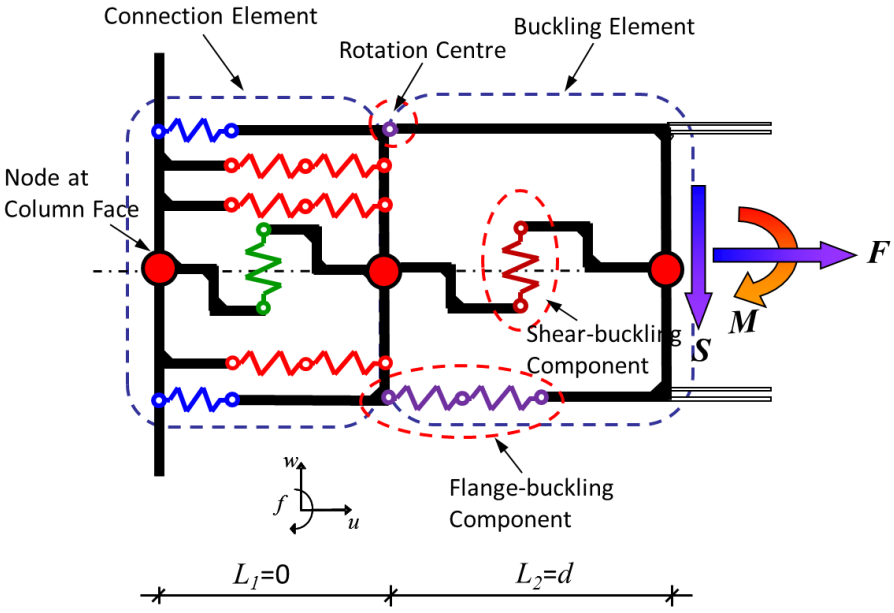

Fig. 26. Component-based connections and beam-end buckling elements.

5. Conclusions

The buckling behaviour of the beam-end bucking zone of a steel beam exposed to elevated temperatures involves three stages: non-linear pre-buckling, plateau and post-buckling. The behaviour of the non-linear pre-buckling stage can be modelled by the existing beam element of Vulcan. In the plateau stage, the ultimate load capacity of the beam-end buckling zone is assumed to be identical to its plastic bending moment resistance. This paper presents a new analytical model to predict

the post-buckling behaviour so that a complete force-deflection relationship of the beam-end bucking zone can be achieved.

The proposed analytical model considers both the beam-web shear buckling and bottom-flange buckling. The interaction between these two buckling modes is accounted for by ensuring compatibility between the out-of-plane deflections of the beam web caused by these two modes. A range of finite element models has been created using ABAQUS. These models were firstly validated against test data, and subsequently used to validate the analytical model. The analytical model has also been compared with Dharma's analytical model. The comparisons have shown that the proposed model provides a reasonably accurate and conservative prediction of the force-deflection relationship for Class 1 and 2 beams, whereas Dharma's model tends to overestimate the post-buckling capacity for beams with slender webs.

This analytical model has then been used to develop a component-based beam-end buckling element, which consists of a web shear buckling component and a bottom-flange buckling component. Each component contains one non-linear spring. The characteristics of each spring have been derived on the basis of the proposed analytical model. This new element is currently being implemented in the software Vulcan to allow performance-based analysis of full-scale structures in fire.

Reference:

[1] Gann RG. Final Report on the Collapse of World Trade Center Building 7,Federal Building and Fire Safety Investigation of the World Trade Center Disaster. Gaithersburg, US: The National Institute of Standards and Technology (NIST); 2008.

[2] Kirby B. The Behaviour of a Multi-Storey Steel Framed Building Subject to Fire Attack-Experimental Data; British Steel Swinden Technology Centre, United Kingdom. 1998.

[3] Burgess I. The Influence of Connections on the Robustness of Composite Structures in Fire. HKIE Fire Division one-day Symposium 2010: Fire Engineering for a Sustainable Future2010.

[4] Burgess I, Davison JB, Dong G, Huang S-S. The role of connections in the response of steel frames to fire. Structural Engineering International. 2012;22:449-61.

[5] Huang S-S, Davison B, Burgess IW. Experiments on reverse-channel connections at elevated temperatures. Engineering Structures. 2013;49:973-82.

[6] Al-Jabri KS, Davison JB, Burgess IW. Performance of beam-to-column joints in fire—a review. Fire Safety Journal. 2008;43:50-62.

[7] Newman GM, Robinson JT, Bailey CG. Fire safe design: A new approach to multi-storey steel-framed buildings: Steel Construction Institute; 2000.

[8] Bailey C, Burgess I, Plank R. Computer simulation of a full-scale structural fire test. Structural Engineer. 1996;74:93-100.

[9] Huang Z, Burgess I, Plank R, REISSNER M. THREE-DIMENSIONAL MODELLING OF TWO FULL-SCALE, FIRE TESTS ON A COMPOSITE BUILDING. Proceedings of the ICE-Structures and Buildings. 1999;134:243-55.

[10] Wang Y. An analysis of the global structural behaviour of the Cardington steel-framed building during the two BRE fire tests. Engineering Structures. 2000;22:401-12.

[11] Block FM, Burgess IW, Davison JB, Plank RJ. The development of a component-based connection element for endplate connections in fire. Fire Safety Journal. 2007;42:498-506.

[12] Yu H, Burgess I, Davison J, Plank R. Tying capacity of web cleat connections in fire, Part 2: Development of component-based model. Engineering Structures. 2009;31:697-708.

[13] Ltd VE. 2015; Retrieved from http://www.vulcan-eng.com

[14] Sun R, Huang Z, Burgess I. A static/dynamic procedure for collapse analysis of structure in fire. Proc Fire Safety Engineering in the UK: The State of the Art (November, 2010). 2010:37-42.

[15] Sun R, Burgess IW, Huang Z, Dong G. Progressive failure modelling and ductility demand of steel beam-to-column connections in fire. Engineering Structures. 2015;89:66-78.

[16] Najjar S, Burgess I. A nonlinear analysis for three-dimensional steel frames in fire conditions. Engineering Structures. 1996;18:77-89.

[17] Cai J, Burgess I, Plank R. A generalised steel/reinforced concrete beam-column element model for fire conditions. Engineering Structures. 2003;25:817-33.

[18] Sun R, Huang Z, Burgess IW. The collapse behaviour of braced steel frames exposed to fire. Journal of Constructional Steel Research. 2012;72:130-42.

[19] Elghazouli A, Izzuddin B. Significance of local buckling for steel frames under fire conditions. 4th International Conference on Steel and Aluminium Structures (ICSAS 99): ELSEVIER SCIENCE BV; 1999. p. 727-34.

[20] Kato B. Buckling strength of plates in the plastic range. Publications of IABSE. 1965;25.

[21] Climenhaga JJ, Johnson RP. Moment-rotation curves for locally buckling beams. Journal of the Structural Division. 1972;98:1239-54.

[22] Gioncu V, Petcu D. Numerical investigations on the rotation capacity of beams and beam-columns. Proceedings of International Colloquim Stability of Steel Structures Further Direction in Stability Research and Design, European Session. 1995;1:163-74.

[23] Gioncu V, Petcu D. Available rotation capacity of wide-flange beams and beam-columns Part 1. Theoretical approaches. Journal of Constructional Steel Research. 1997;43:161-217.

[24] Gioncu V, Mazzolani F. Ductility of seismic-resistant steel structures: CRC Press; 2003.

[25] Dharma RB, Tan K-H. Rotational capacity of steel I-beams under fire conditions Part II: Numerical simulations. Engineering Structures. 2007;29:2403-18.

[26] Dharma R, Tan K. Experimental and numerical investigation on ductility of composite beams in the Hogging moment regions under fire conditions. Journal of structural engineering. 2008;134:1873-86.

[27] Timoshenko SP, Gere JM. Theory of elastic stability. 1961. McGraw-Hill, New York; 1961.

[28] CEN. BS EN 1993-1-1. Design of steel structures. Part 1.1: General structural rules. UK: British Standards Institution; 2005.

[29] Dharma RB. Buckling behaviour of steel and composite beams at elevated temperatures 2007.

[30] Huang Z, Burgess IW, Plank RJ. 3D Modelling of Beam-columns with General Cross-sections in Fire. Paper S6-5, Third International Workshop on Structures in Fire, Ottawa, Canada2004. p. p323-34.

[31] Dharma RB, Tan K-H. Rotational capacity of steel I-beams under fire conditions Part I: Experimental study. Engineering Structures. 2007;29:2391-402.

[32] Quan G, Huang S-S, Burgess I. An analytical approach to modelling shear panels in steel beams at elevated temperatures. Engineering Structures. 2015;85:73-82.

[33] Hencky H. Zur Theorie plastischer Deformationen und der hierdurch im Material hervorgerufenen Nachspannungen. ZAMM ‐ Journal of Applied Mathematics and Mechanics/Zeitschrift für Angewandte Mathematik und Mechanik. 1924;4:323-34.

[34] Hibbit D, Karlsson B, Sorenson P. ABAQUS reference manual 6.7. Pawtucket: ABAQUS Inc; 2005.

[35] CEN. BS EN 1993-1-2. Design of steel structures. Part 1.2: General rules — Structural Fire Design. UK: British Standards Institution; 2005.

[36] Torić N, Sun RR, Burgess IW. Testing the acceptability of different creep strain calculation models in structural fire analysis. 8th International Conference on Structures in Fire2014.

List of Tables

List of Figure Captions